

Deep Space Relay Architecture for Communication and Navigation

Paul Carter¹ and E. Glenn Lightsey²
Georgia Institute of Technology, Atlanta, Georgia, 30318

The Deep Space Relay architecture explored in this paper is intended to provide communication and navigation services to Mars surface users and spacecraft in the Mars vicinity. The relay orbiters making up this architecture will be placed in strategic heliocentric orbits near Mars so as to mitigate the Mars superior conjunction problem for optical communications, and at the same time provide a good geometry for deep space navigation. Design trades are performed to ensure that the relay architecture is optimal in its roles as both a communication provider and navigation provider. Geometric constraints are identified that allow the relay architecture to provide continuous optical link coverage throughout the time period from 2030-2060. An optimal and minimal relay architecture is identified that meets these geometric constraints while also maximizing the data return of the optical link and providing a suitable geometry for trilateration-based navigation with the fewest relay orbiters possible. The communication performance of this optimal relay geometry is assessed through an analysis of the additional access time and data return it provides. On the navigation side, the performance of the optimal architecture is assessed based on access and a geometric dilution of precision (GDOP) analysis. An expanded architecture is introduced which adds a relay in a Mars halo orbit to the minimal architecture for additional communication and navigation benefits.

I. Nomenclature

| | | |
|----------------|---|---------------------------------|
| <i>DSN</i> | = | Deep Space Network |
| <i>RF</i> | = | Radio Frequency |
| <i>DSAC</i> | = | Deep Space Atomic Clock |
| <i>SWaP</i> | = | Size, Weight, and Power |
| <i>DWE</i> | = | Direct-with-Earth |
| <i>SEP/SPE</i> | = | Sun-Earth-Probe/Sun-Probe-Earth |
| <i>SDSN</i> | = | Space-based Deep Space Network |
| <i>PPM</i> | = | Pulse Position Modulation |
| <i>SNR</i> | = | Signal-to-Noise Ratio |
| <i>JDR</i> | = | Joint Doppler and Ranging |

II. Introduction

Currently, deep space missions beyond the Moon are all robotic missions. For their communication needs, these missions either rely on large Earth-based antenna apertures (e.g., Deep Space Network (DSN) stations) to directly communicate with the spacecraft, or in the Mars case, may also utilize Mars-orbiting relays³ to provide proximity communications with a spacecraft on the Mars surface or in Mars orbit. In both cases, current Mars missions, which utilize X-band and Ka-band radio frequencies (RF), experience 1-2 week communication outages during Mars

¹ Graduate Research Assistant, Daniel Guggenheim School of Aerospace Engineering, pcarter6@gatech.edu

² Professor, Daniel Guggenheim School of Aerospace Engineering, glenn.lightsey@gatech.edu

³ Currently operational Mars relay orbiters include the Mars Reconnaissance Orbiter, Odyssey, MAVEN, Mars Express, and ExoMars Trace Gas Orbiter.

superior conjunction⁴. As deep space missions shift their communications into optical frequencies, the outage times during conjunction periods will grow significantly. For their navigation needs, deep space missions currently use a non-real-time navigation process. In this process, received tracking measurements (typically from the DSN) are compared against expected tracking measurements, which are calculated based on the nominal trajectory of the spacecraft and an appropriate measurement model. The residuals between the received and expected measurements are then used to iteratively refine knowledge of the spacecraft's true trajectory [1]. These communication and navigation paradigms have been suitable for past and contemporary deep space robotic missions, however future deep space missions, particularly human missions, will levy more stringent requirements on communication coverage, redundancy, and data return and on the timeliness and accuracy of position and velocity estimations. This motivates demand for the deep space relay architecture explored in this paper.

An enabling assumption for this relay architecture investigation is that it will be technically and fiscally possible to place multiple relay spacecraft into the deep space orbits considered in this study. It is also assumed that it will be possible for the relays to perform the station keeping maneuvers needed to maintain these orbits. These relays will need to be large in order to accommodate sufficiently sized antennas and optical communications payloads for communication at deep space distances. They will also require suitably stable oscillators in order to provide radiometric tracking measurements that can be used for navigation. Several recent developments in the space industry have made deployment of relay platforms that meet these assumptions technically and fiscally feasible for the near future:

1. Availability of cost competitive and heavy lift cargo services for deep space – one example is SpaceX's Starship, which is designed for human and cargo missions to the Moon and Mars. According to the Starship User Guide [2], the Starship platform can carry 100+ tons of payload to Mars and has an 8-meter diameter payload envelope. An extended payload volume is also available for payloads requiring up to 22-meters of height. The unique and large geometry of the Starship payload bay and its heavy lift capabilities would allow for the stacking of multiple relay spacecraft with large antenna dishes and optical payloads into the rocket's payload bay, and the ability to deploy the satellites into different deep space orbits, all on a single launch.
2. Solar Electric Propulsion – many deep space missions now carry solar electric propulsion systems for cruise and orbit-phasing operations. One example is the Psyche spacecraft, which carries four SPT-140 Hall-effect thrusters [3]. These propulsion systems allow for efficient orbit phasing, thus enabling a variety of relay geometries with minimal propellant, which is an important operation consideration for the deep space relay concept as will be show later in the paper. The large solar panels needed for the solar electric propulsion system can also help to generate the high power needed for deep space optical communications.
3. Deep Space Atomic Clock (DSAC) – the DSAC is an ultra-precise mercury-ion atomic clock designed for use in deep space. In its 2019 technology demonstration mission, the DSAC demonstrated sufficient stability for enabling one-way radiometric tracking measurements. This means that a navigating spacecraft can make in-situ range and doppler measurements from an uplinked tracking signal rather than needing to rely on traditional two-way DSN tracking methods, thus making near-real-time deep space positioning possible [4].

III. Relay Architecture Description

To help meet increased communication and navigation demands in the upcoming era of deep space exploration (i.e., 2030-2060) and to leverage on recent enabling technologies, this paper explores a deep space relay architecture that provides communications and navigation services for spacecraft in the Mars vicinity and in the inner-planets region. The deep space relay orbiters making up this architecture will carry both RF and optical frequency communication payloads and will be placed in strategic Mars heliocentric orbits that mitigate the Mars superior conjunction problem for optical communications [5]. The relay architecture configuration will also be chosen to provide good geometry for deep space positioning. The main focus of this paper is a relay architecture involving 2 relay orbiters; one in a heliocentric, Mars-leading orbit inclined with respect to the Mars orbital plane, and the other in a heliocentric, Mars-trailing orbit inclined equally in the opposite direction (see Figure 1).

⁴ Mars superior conjunction occurs when Earth and Mars are on opposite sides of the Sun, thus a direct link between the two planets is obstructed by the Sun.

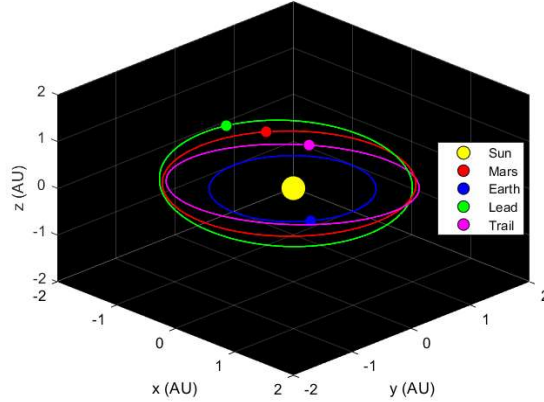


Figure 1. Orbital geometry of the combined leading and trailing Deep Space Relay architecture.

Under the right geometric conditions (which are derived in Section IV), this relay architecture is advantageous for both communication and navigation. For communication, the leading/trailing geometry of the architecture allows for continuous communication with Mars users during conjunction periods. Through the combination of one leading and one trailing relay, the architecture is able to solve the conjunction problem while minimizing the Mars-relay distances. The Mars user-relay proximity links involve two space-based terminals and are thus more constrained in size, weight, and power (SWaP), thus minimizing the Mars-relay distances is advantageous for the data return of the overall architecture. For navigation, the combination of two relays plus an Earth station provides the three range measurements needed for the deep space trilateration method discussed in Section VI. The inclined orbit planes of the relays ensure that there is sufficient geometric diversity of measurements for navigating users.

In this paper, a static relay architecture will be assumed so that an optimal relay geometry can be identified with respect to both communication and navigation performance. However, it is envisioned that the relay architecture could be reconfigurable, meaning that the relay orbiters can execute orbit-phasing operations to get closer to or farther from Mars, depending on the instantaneous communications and navigation needs of its users. The concept of operations for these maneuvers will be discussed in Section IV.

A. Communication

One key objective of this paper is to investigate using the deep space relays to ensure communication continuity with Mars users during Mars superior conjunction and to improve the overall data return. Mars superior conjunction occurs once per Mars synodic period (~ 780 days) when Earth and Mars are on opposite sides of the Sun. This event creates an extended period of both RF and optical communications disruption between Earth and Mars due to an increase in solar background noise seen at receiving antennas and an increase in charged particles in the path of the propagating signals [6]. The exact details of the communication disruption depend on the geometry of the Sun, Earth, and Mars during a particular conjunction, as well as the telecommunication hardware, link frequency, and requirements of the given mission.

Past and present robotic missions, whose communications have primarily been RF, have typically dealt with the conjunction problem by implementing a communication moratorium lasting 1-2 weeks. However, many future Mars missions, particularly crewed missions, will have a need to communicate reliably even during conjunction. Furthermore, future missions will increasingly rely on optical communication, which offers significant data return improvements over RF, but is also more sensitive to background noise from the Sun, thus resulting in longer communication outage times during conjunction. The sensitivity of optical communication to solar background noise can also create scenarios in which communication must be suspended during Mars opposition⁵ as well. These outages are shorter than the outages during conjunction but are still undesirable from a data return point of view because Earth and Mars are at their closest during opposition, a situation which normally results in the highest possible data return.

⁵ Mars Opposition is when Mars and Earth are on the same side of the Sun.

To mitigate the Mars conjunction problem for optical links, this paper explores a relay architecture which allows all Mars users to have continuous communications access to Earth. This is accomplished through a direct-with-Earth (DWE) link when Mars is not in conjunction or opposition, and through a two-hop relay link when the direct link is geometrically infeasible. The two-hop relay link would consist of forward and return relay links between Earth and the relay, and forward and return proximity links between the relay and the Mars user, which could be either a Mars surface user or a Mars orbiter. Conjunction and opposition conditions are essentially equivalent for both user cases. Figure 2 provides a schematic of these links.

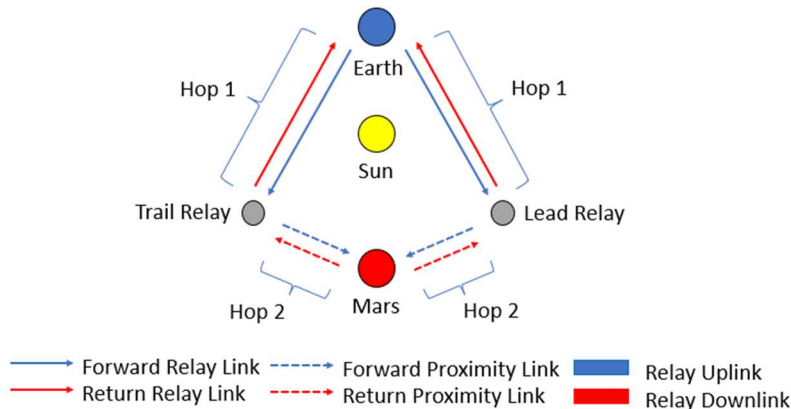


Figure 2. Deep Space Relay architecture link schematic (the bodies shown are orbiting the Sun in the counterclockwise direction).

This paper seeks to identify the relay geometry that will not only ensure communication continuity, but also maximize the optical data return. Thus, a geometrical balance must be struck between providing sufficiently large Sun-Earth-Probe (SEP) and Sun-Probe-Earth (SPE) angles to minimize the solar noise power in the optical channel and minimizing the hop distances for the more SWaP constrained proximity links. With the right balance of these two considerations, the relay geometry will not only provide continuous coverage, but will also ensure that the pulse position modulated (PPM) optical link operates in its signal-power dominated regime, in which the link’s capacity falls off with R^2 and avoids the noise power dominated regime, in which the capacity falls off with R^4 (where R is the range between transmitter and receiver) [7]. The optical link capacity is discussed in detail in Section V. In addition to optical communications, the relay orbiters in this architecture will also support RF communications in the Ka-band to provide communications redundancy and for radiometric navigation signals. Given that optical links have more stringent SEP and SPE angle requirements than the RF links due to their higher sensitivity to solar noise, a relay architecture providing full coverage for optical links is guaranteed to provide full coverage for RF links as well.

B. Navigation

The two relay orbiters, when used in combination with Earth’s DSN stations, will form a Space-Based Deep Space Network (SDSN) that provides the needed geometric diversity of tracking measurements to support near-real-time navigation of users in the space service volume covering the Mars vicinity and the inner-planets region. To provide this navigation service, this paper considers the use of radiometric and/or optometric range measurements between a user spacecraft and the various assets in the SDSN for a trilateration positioning scheme. The term “near-real-time” is used here because the timeliness of the range measurement, and thus the position fix itself, is limited by the light-time delay and whether or not 1-way or 2-way measurements are employed. The 1-way light time between Earth and Mars ranges between 4 minutes and 24 minutes. There are 3 potential ranging approaches that could be employed, depending on the capabilities of the user spacecraft:

1. 2-way ranging scheme in which with the relay orbiters and Earth stations transmit a ranging signal to the user spacecraft, which then transponds the signal back to the respective transmitting terminal where the range measurement is actually made. In this case, a round-trip light-time is required for the relay or DSN station to make the range measurement and an additional 1-way light-time is required to send the range estimate back to the user.

The measurement complexity of this scheme primarily lies with the relay orbiters and DSN stations, which is desirable if the user spacecraft is lacking in signal processing or computational abilities. However, the drawback of this scheme is that it is the least timely, requiring 3 total 1-way light-times in order to generate a single range measurement. The 2-way nature of this scheme means that only one clock is involved in the range measurement, thus trilateration can be performed with only 3 measurement nodes because no clock bias must be solved for.

2. 2-way ranging scheme in which with the user spacecraft transmit a ranging signal to the relay orbiters and Earth stations, which then transpond the signal back to the user spacecraft where the range measurement is actually made. In this case, one round-trip light-time is required for the use spacecraft to make the range measurement. The measurement complexity of this scheme primarily lies with the user spacecraft; thus, the user would need to have sufficient hardware capability to perform the necessary signal processing for making a 2-way range measurement. This method is more complicated for the user, but more timely than the previous 2-way ranging scheme, requiring only 1 round-trip light-time to generate a single range measurement. Again, the 2-way nature of this scheme allows for trilateration with only 3 measurement nodes.

3. 1-way ranging scheme in which the relay orbiters and Earth transmit a ranging signal to the user spacecraft, which processes the range measurement in-situ. In this scheme, the relays and Earth stations could broadcast out a common ranging signal which could be received by multiple users. Again, the measurement complexity in this case lies with the user spacecraft, which would require a DSAC in order to perform the one way ranging measurement [4]. This scheme is the most timely, with the range measurement being made instantaneously at the user end upon reception of the signal. However, because this is a 1-way ranging scheme, trilateration using these range measurements would require resolving an unknown clock bias between the infrastructure elements of relay orbiters and Earth. Thus, a fourth network node would be required for this scheme.

Section VI of this paper considers a minimal (i.e., 3 node) trilateration approach for navigation of users in the Mars vicinity. This approach is essentially a deep space version of the trilateration positioning commonly used by Global Navigation Satellite Systems (GNSS) [8]. To perform the trilateration, three total 2-way range measurements are used: one to or from the leading relay, one to or from the trailing relay, and one to or from Earth. This minimal approach could leverage either the first or second ranging scheme listed above. With the addition of a 3rd relay, trilateration for Mars users could be accomplished using the 1-way ranging scheme discussed above. This is highly desirable from an operational standpoint as many Mars users could be supported by a single ranging signal broadcasted from each node in the SDSN. Navigation via a deep space trilateration method allows the user to produce a 3-D kinematic position fix. The latency of this position fix relative to the transmit time of the ranging signal depends on the light-time between the SDSN node and the user and which ranging scheme is being used. In the worst cases (i.e., near conjunction using the first 2-way ranging scheme), the latency is on the order of ~ 1 hour. This is still a significant improvement from a timeliness perspective over traditional DSN tracking techniques, which can require the accumulation of days of tracking measurements to estimate position.

For providing navigation to users in the inner-planets region and relatively close to Earth, the Deep Space Relay architecture would utilize a novel relative positioning technique known as double-differencing joint doppler ranging (DD-JDR) [9]. This technique involves double-differencing of 1-way range measurements and Doppler measurements from the two relay orbiters and received by Earth and the spacecraft respectively, and a 2-way range measurement between Earth and the spacecraft. Together, these three measurements provide a 3-D near-real-time position estimation of the spacecraft relative to Earth. This navigation method is outside of the scope of this paper but is discussed in the context of the Deep Space Relay architecture in a companion paper [10].

IV. Geometric Considerations for the Deep Space Relay Architecture

A. SEP/SPE Angle Challenges for Communication

The Sun-Earth-Probe (SEP) angle and Sun-Probe-Earth (SPE) angles are important geometrical parameters for quantifying the effects of conjunction and opposition on communication links. The term “probe” here refers to the object the Earth is communicating with for a given link. For the purposes of analyzing the DWE link, the SEP and SPE angle refer to the Sun-Earth-Mars and Sun-Mars-Earth angles respectively. Similarly, for the purposes of analyzing the relay links, the SEP and SPE angles refer to the Sun-Earth-Relay and Sun-Relay-Earth angles

respectively. For downlinks from the Mars user or a relay to Earth, the SEP angle is the parameter of interest, because it describes the angle between the Sun and the Mars user or relay transmitting antenna as seen from the receiving antenna on the Earth. Likewise, for uplinks from the Earth to a Mars user or a relay, the SPE angle is the parameter of interest, because it describes the angle between the Sun and the transmitting antenna on Earth, as seen from the Mars user or relay receiving antenna. Poor link geometry occurs when the SEP and SPE angles are low because these are the times in which it becomes difficult or impossible to close the link. Figure 3 illustrates the low SEP and SPE angle situations that occur during Mars conjunction and opposition.

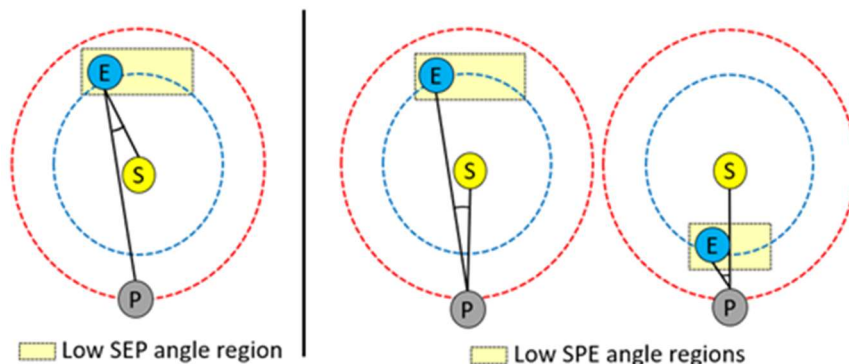


Figure 3. Low SEP and SPE angle geometries. The leftmost and middle plots correspond to conjunction, which results in both a low SEP and SPE angle. The rightmost plot corresponds to opposition, which results in a low SPE angle, but a large SEP angle.

For links during conjunction, both the SEP and SPE angles are low, and the transmitted signals must physically pass near the Sun. Thus, there are two effects that can potentially diminish the link performance during conjunction: scintillation and solar noise [6]. The scintillation effect refers to the degradation (i.e., fading) of the signal due to solar charged particles in the propagation path. This fading decreases the likelihood of the signal's message being detected correctly. The solar noise effect refers to the noise power picked up by the receiving antenna when pointed near the disk of the Sun. This noise degrades the received signal-to-noise ratio, which decreases the achievable data rate of the link. During opposition, the signal does not pass near the Sun, so the solar scintillation effect is no longer a factor. However, for uplinks from Earth to the Mars user or relay during opposition, the low SPE angle means that the Sun will still be angularly close to the Earth in the field of view of the receiver, thus the solar noise effect is still relevant during opposition.

SEP and SPE angle cutoffs are employed in link analysis as a practical means of determining when a link is geometrically infeasible. These cutoffs capture the scintillation and solar noise effects on the link and are dependent upon the frequency of the link they apply to. RF links are more robust to solar noise effects, but more sensitive to scintillation effects compared to optical links. Typical SEP/SPE cutoffs for RF links are 2.3° for X-band and 1° for Ka-band [6]. The cutoffs for these RF links are driven primarily by the scintillation effect; thus, they are relevant during conjunction but not opposition. While optical links are not as sensitive to the scintillation effect, they are still much less tolerant to low SEP/SPE angles because they are highly sensitive to noise photons received from the Sun. As the SEP angle decreases, the amount of noise power due to incident solar noise photons increases dramatically, eventually pushing the optical link into unacceptable performance regimes [7]. To account for this, typical optical downlink cutoffs are 10° for SEP angle and 3° for SPE angle. The cutoffs for optical links are driven by the solar noise effect; thus, they are relevant during both conjunction and opposition. The SPE angle cutoff is relevant even in the optical downlink case to account for the uplink acquisition beacon that is needed to enable sufficiently accurate pointing of the downlink beam. Given that the optical downlink has both the largest SEP and SPE angle cutoffs, the optical downlink provides the dominant geometrical constraint on the relay architecture. Thus, 10° and 3° will be used as the SEP and SPE angle cutoffs respectively in the following analysis to determine viable relay architectures.

B. Conjunction and Opposition Outages

The amount of time that the SEP or SPE angle of the DWE link is below its cutoff (i.e., the amount of link outage time) depends on the exact geometry of the given conjunction or opposition period. Conjunction and opposition for

Mars and for the relays occur once every Mars synodic period (~780 days). Depending on the location of Earth and Mars along their respective orbits, the conjunction and opposition periods can vary in length, and vary in the minimum SEP and SPE angles during that specific event. These variations affect the duration of the communications outages that are experienced for a given link at a given time. Through SPICE simulation of the Sun-Earth-Mars geometry, the outage times for each DWE link type were computed and are shown for conjunction and opposition periods during the 2030-2060 time window in Table 1. Note that the conjunction and opposition period start dates are defined as the first point when the SEP or SPE angles dip below their respective optical link thresholds (if at all). The significant outage periods for optical links in the 2030-2060 time period, which range from about 60-91 days, are clearly not acceptable for future human Mars missions. This is a key motivation for implementing a relay architecture to provide an alternate communication path for Mars users.

Table 1. DWE link outage times.

| Conjunction Period Start | Optical Link Outage Time (days) | Ka-band Link Outage Time (days) | Opposition Period Start | Optical Link Outage Time (days) |
|--------------------------|---------------------------------|---------------------------------|-------------------------|---------------------------------|
| 4/14/2030 | 78.3 | 7.5 | 5/1/2031 | 6.9 |
| 6/7/2032 | 66.5 | 1.3 | 2033 | 0.0 |
| 7/19/2034 | 61.0 | 0.0 | 2035 | 0.0 |
| 8/24/2036 | 60.0 | 3.0 | 11/16/2037 | 6.4 |
| 10/1/2038 | 63.4 | 6.2 | 12/31/2039 | 4.3 |
| 11/12/2040 | 74.1 | 5.5 | 2/5/2042 | 3.0 |
| 1/8/2043 | 90.8 | 0.0 | 3/9/2044 | 4.5 |
| 3/19/2045 | 84.5 | 8.4 | 4/14/2046 | 6.5 |
| 5/19/2047 | 70.2 | 4.4 | 5/31/2048 | 5.8 |
| 7/3/2049 | 62.5 | 0.0 | 2050 | 0.0 |
| 8/11/2051 | 59.8 | 0.0 | 10/25/2052 | 6.1 |
| 9/16/2053 | 61.4 | 5.3 | 12/15/2054 | 5.3 |
| 10/26/2055 | 68.8 | 6.5 | 1/22/2057 | 3.2 |
| 12/14/2057 | 85.1 | 0.0 | 2/25/2059 | 3.7 |

C. Leading/Trailing Relay Architecture

Several relay satellite architectures have been proposed in the literature to circumvent the issue of Mars conjunction link outage. Reference [11] considers a class of kidney-bean shaped Trojan orbits around the Sun-Mars L4/L5 points which can provide continuous Earth-Mars communications during solar conjunction periods. However, these relay orbiters are considerably far from Mars (~1.5 AU), which results in a prohibitive telecom burden on the SWaP constrained proximity links. Several other choices of relay satellite orbits were proposed in [5] to bridge the solar conjunction gaps. These include Earth-Sun L3/L4/L5, Mars-Sun L4/L5, and Mars lead/trail relay orbits. This paper focuses on deep-space relay satellites in Mars leading and trailing inclined orbits. As their names indicate, these are heliocentric orbits traveling along with Mars, but leading or trailing it by some Mars-Sun-Relay separation angle and inclined with respect to the Mars orbit plane by some inclination angle. A plot of these relay orbits was shown in Figure 1.

The leading/trailing relay orbits considered in this paper stand out from the orbits discussed in [5] and [11] because they allow the flexibility to control the separation between the relays and Mars. Thus, in this study, the Mars-Sun-Relay angle can be optimized so that the Earth can always communicate with Mars via the leading and/or trailing relay orbiters during any solar conjunctions, while also maintaining favorable ranges for the proximity links. In this analysis, it is assumed that the relays follow the same orbits as Mars, but with their true anomalies shifted relative to Mars based on the desired Mars-Sun-Relay angle. The true anomaly is shifted forward for the leading relay and backwards for the trailing relay. This true anomaly shifting method was implemented in simulation by mapping the desired Mars-Sun-Relay angle to a time shift of the Mars ephemeris based on the Mars orbital period. The ephemeris of Mars at the corresponding time shift (shifted forward for the leading relay and backwards for the trailing relay) was then used as

the ephemeris for the relay. Due to the eccentricity of the Mars orbit, this time shifting method results in instantaneous Mars-Sun-Relay angles that oscillate around the commanded Mars-Sun-Relay separation angle with a period equal to the Mars orbit period. This is illustrated in Figure 4 for two different commanded separation angles. As can be seen from the figure, larger commanded separation angles result in larger deviations from the commanded angle.

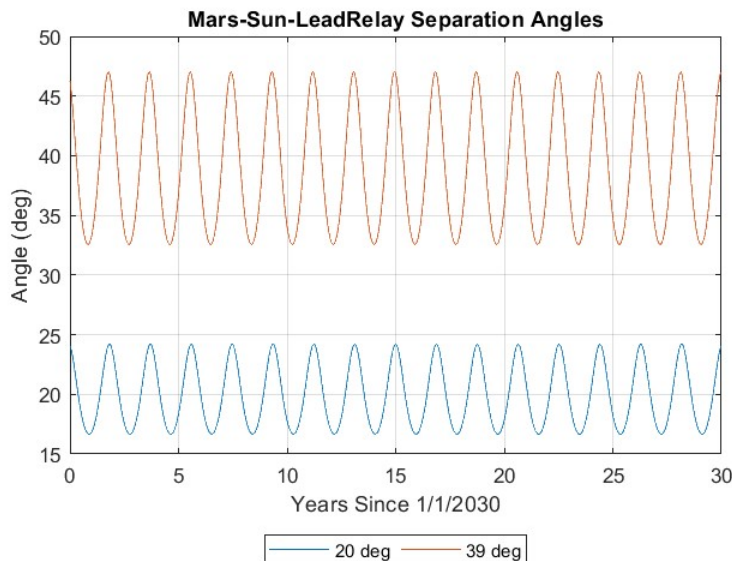


Figure 4. Oscillations of the instantaneous Mars-Sun-Relay separation angle about the commanded separation angle for 20° and 39° leading relays.

D. Optimal Relay Geometry

The identification of an optimal relay geometry with respect to communication performance starts with finding the relay geometries that satisfy the geometric constraints imposed by the optical link SEP/SPE angle cutoffs. Such relay geometries will enable continuous geometrical access to Mars during periods of Mars conjunction and opposition for all link types. To satisfy the SEP/SPE angle geometric constraint, the Sun-Earth-Relay and Sun-Relay-Earth angles of a given candidate relay geometry must be greater than the optical downlink SEP and SPE angle cutoffs respectively for all times during which the DWE optical downlink is geometrically infeasible (i.e., during Mars conjunctions and some oppositions). In other words, a viable relay geometry must provide a relay link with SEP angles larger than 10° for all conjunction times during which the Sun-Earth-Mars angle is less than 10° and must provide a relay link with SPE angles larger than 3° for all opposition times during which the Sun-Mars-Earth angle is less than 3° .

Analytical expressions for the Mars-Sun-Relay separation angle required to ensure continuity of coverage during Mars conjunction have been derived and produce a minimum separation angle of $\sim 33.3^\circ$ for a single relay architecture coplanar with the Mars orbit [11]. The analytical approach assumes that the Earth and Mars have coplanar, circular orbits with orbit radii of 1 and 1.5 AU respectively. Thus, the analytical method provides a useful reference value, but fails to capture the reality of the Sun, Earth, Mars geometry over the course of different synodic periods and is unable to handle inclined relay orbits. To account for this, a direct SPICE geometry simulation of the ephemeris for all relevant bodies was employed. Relay separation angles were simulated in 1° increments and iterated over in order to find the separation angles that enable continuous coverage during the 2030-2060 time period. Figure 5 show the maximum number of days during any of the Mars conjunction or opposition periods from 2030-2060 for which the relay SEP and SPE angles are below their respective optical thresholds for (1) a single leading relay, (2) a single trailing relay, and (3) a symmetric combination (i.e., equal separation angles) of one leading and one trailing relay, all of which are assumed in this plot to be coplanar with the Mars orbit. From this plot, the geometric requirements for continuous coverage during conjunction in the non-inclined case are observed based on the points at which each architecture reaches 0 days of both SEP and SPE angle constraint violation. For the single lead and trail architectures, continuous coverage is guaranteed with a commanded Mars-Sun-Relay separation angle of at least 39° . This value is larger than the value derived analytically for 3 reasons: first, the quantization of the design space into 1° increments

results in the true threshold being rounded up; second, this simulation accounts for the eccentricities and relative inclinations of Earth and Mars; and third, and most importantly, the instantaneous Mars-Sun-Relay separation angle oscillates about the commanded separation angle with a period incoherent to the Mars synodic period (as shown in Figure 4). For the symmetric, combined leading and trailing architecture, the minimum commanded relay separation angle to guarantee continuous coverage drops down to just 20° . Another insight to be gained from Figure 4 is that the SPE angle constraints are satisfied at lower relay separation angles than the SEP angle constraint. Thus, any geometry satisfying the SEP angle constraint during conjunction is guaranteed to also satisfy the SPE angle constraints at conjunction and opposition as well. So going forward, only the SEP angle constraints during conjunction must be considered in the search for the optimal geometry.

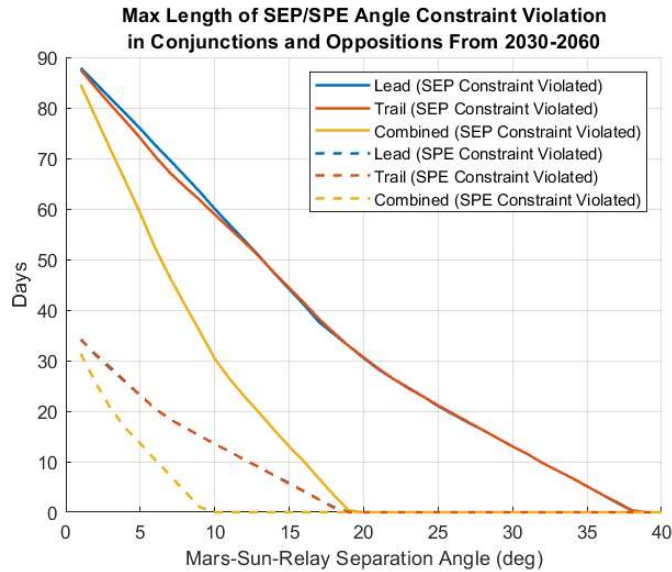


Figure 3. Maximum length of outage times during conjunction and oppositions based on the satisfaction of the SEP and SPE angle constraints for different commanded relay separation angles.

The coplanar relay orbits just considered are sufficient for meeting the communication goals of the relay architecture, but not the navigation goals, because they lack geometric diversity in the orthogonal direction to the ecliptic plane, as will be discussed in more detail in Section VI. To provide this needed geometric diversity, the relay orbits must be inclined with respect to the Mars orbit plane. This is accomplished in simulation by first time shifting the Mars ephemeris based on the desired commanded separation angle. Then, the resulting ephemeris is rotated by the desired inclination angle about the Mars orbit line of nodes vector. This rotation is done by a positive angle for the leading relay and a negative angle for the trailing relay. The coplanar analysis performed above does serve to down select the design space of separation angles that must be iterated over for each inclination angle considered, which is enabling from a computational perspective. From the coplanar results, it can be seen that single relay architectures require very large relay separation angles, which results in prohibitively large Mars-relay distances for the proximity link. Thus, only combined leading/trailing architectures are considered for the rest of the analysis. It is also noted that, given the simulation approach just described for the inclined relay geometries, the addition of an inclination with respect to the Mars orbit plane will serve to increase the instantaneous Mars-Sun-Relay separation angles beyond those of the coplanar case for the same commanded separation angle. Thus, the maximum commanded separation angle needed to be considered is 20° , as any inclination will serve to drive this number down.

To search for the relay geometries enabling continuous coverage over the dimensions of both relay separation angle and inclination angle, a direct simulation was implemented, in which combined leading and trailing architectures were generated with relay inclination angles varying from 0° to 40° degrees with an angular resolution of 1° , and Mars-Sun-Relay separation angles varying from 0° to 20° with an angular resolution of 1° . Figure 6 displays a sampling of these separation angle/inclination angle combinations and their associated maximum outage lengths during conjunctions from 2030-2060.

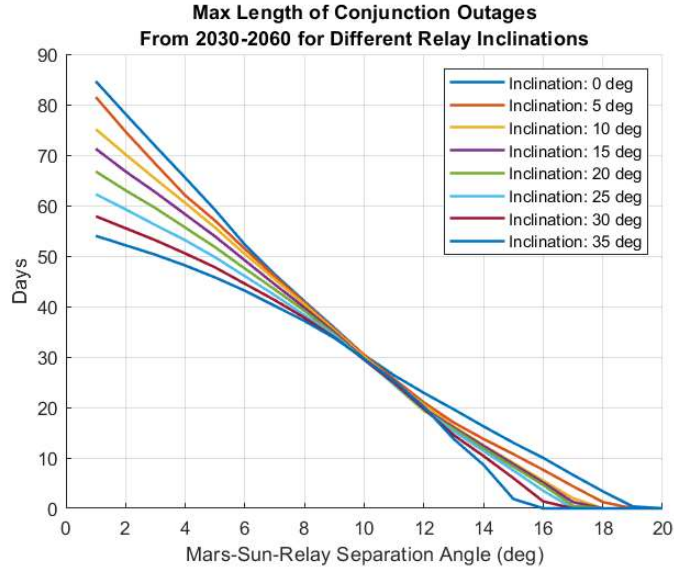


Figure 6. Maximum conjunction outages for a variety of relay separation angle and inclination angle combinations.

As expected, the higher the inclination of the relay orbits and the larger the Mars-Sun-Relay separation angle, the more the solar conjunction gaps are reduced. However, the rates are not linearly correlated. For example, at 0° inclination, to maintain the SEP angle above the 10° threshold, the commanded Sun-Mars-Relay separation angle must be at least 20° . Inclining the relay orbits by 10° , drops the minimum commanded separation angle needed for continuous coverage down to 18° . The jump from 10° to 30° inclination only serves to drop the necessary separation angle down to 17° . This behavior is due to the fact that twice in a Martian year, the relay orbiters enter Mars’ orbital plane at their ascending and descending nodes. Solar conjunctions occasionally happen at these times; thus, the impact of inclination becomes less significant for these particular conjunction periods.

While adding inclination to the relay geometry serves to add geometric diversity for navigation, excessive orbit inclination adversely pushes the relay orbiters further from Mars, thus placing more burden on the SWaP constrained proximity links. To find an optimal balance between relay separation angle, inclination angle, and proximity link range, the same grid of separation and inclination angles described above was iterated over and the corresponding geometric constraints and maximum proximity link distances during the 2030-2060 time period were calculated and plotted in Figure 7. The inclination-proximity link range tradeoff is clearly visible in this plot. At the uninclined, 7° Mars-Sun-Relay separation angle mark, the distance between the relay orbiters and Mars is less than 0.2 AU. By inclining the orbit plane of this commanded separation angle 35° , the Mars to relay orbiter distance grows five times further. A jagged red line is plotted in Figure 7 to capture the SEP angle constraints. Valid geometries (i.e., geometries that guarantee continuous coverage) exist to the right of the red line. The optimal geometry can be identified in this plot by finding the shortest Mars-relay range (i.e., the lowest contour) where all coverage criteria are met (i.e., to the right of the red line). This geometry is indicated by a star on the plot and corresponds to a commanded Mars-Sun-Relay angle of 18° and an inclination angle of 10° . With this relay geometry choice, the SEP/SPE angle constraints are met for all time (continuous communication from 2030-2060), the relay orbiters are sufficiently inclined (diverse geometry for range measurements), and the Mars to relay orbiter distance is no more than ~ 0.5 AU (reduces telecom burden on SWaP constrained Mars users and relays).

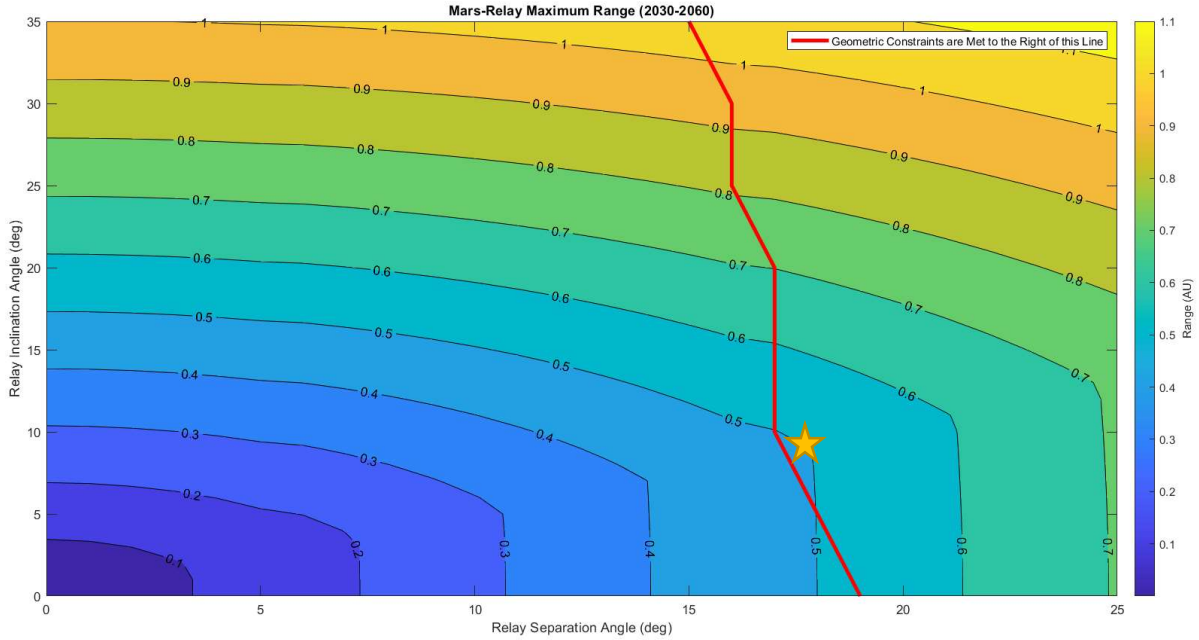


Figure 7. Maximum Mars-Relay distances for different inclinations and relay separation angles. The red line in the plot shows where SEP angle conditions are met for all of 2030-2060. Continuous communications are possible in the regions to the right of the red line. The star indicates the optimal relay geometry.

Figure 8 (on the next page) illustrates the evolution of the SEP angle for the relay and DWE links during each conjunction period from 2030-2060 for the optimal relay geometry just identified. It can be seen that for all times at which the Mars user SEP angle is below the optical threshold, either the leading or trailing relay SEP angle is above its threshold, thus ensuring continuity of coverage. This figure gives an indication of how conjunction would be handled by a Mars user operationally. As the Mars user enters conjunction, the DWE link is no longer geometrically feasible, but the lead relay link is geometrically feasible. Thus, communications with Earth would occur via the Mars user linking to the lead relay, which would then forward the link along to Earth. Eventually, the lead relay link SEP angle dips below the optical threshold and becomes unfeasible as well, but as this time, the SEP angle of the trail relay link is guaranteed to have risen back above the optical threshold. The Mars user would then switch from the lead relay to the trail relay to maintain its communication path to Earth. This path would then be used until the time at which the Mars user SEP angle rises back above the optical threshold, thus allowing the DWE link to be used once again.

E. Propulsion Requirements and Architecture Reconfiguration

To maintain the required relay separation angles for the optimal relay geometry, the relay orbiters must constantly propel themselves from Mars to nullify its gravitational perturbations on their heliocentric orbits. Propulsion analysis performed in a companion relay architecture paper showed that maintaining the optimal relay geometry requires a maximum constant thrust of ~ 0.01 mN [10]. Mars-Sun-Relay separation angles of 5° require a maximum constant thrust of ~ 0.13 mN due to their closer proximity to Mars. In both cases, the required thrust level can be easily achieved using the smallest current commercially available solar electric propulsion system: the BHT-200 developed by BUSEK, which can produce up to 13 mN of constant thrust [12].

The station-keeping propulsion requirements just described ensure that the architecture can preserve the Mars-Sun-Relay separation angles required for continuous coverage and geometric diversity. However, during non-conjunction and non-opposition times, it may be desirable to use additional maneuvers to reconfigure the architecture to better suit the needs of the Mars users and/or interplanetary users at a given time. For example, there may be times when it is advantageous to move the relays much closer to Mars to alleviate telecom burden on small Mars users, thus improving their data return. There may also be times it is advantageous to move the relays further from Mars and/or increase their inclination in order to further diversify the navigation geometry, thus providing a better position fix for

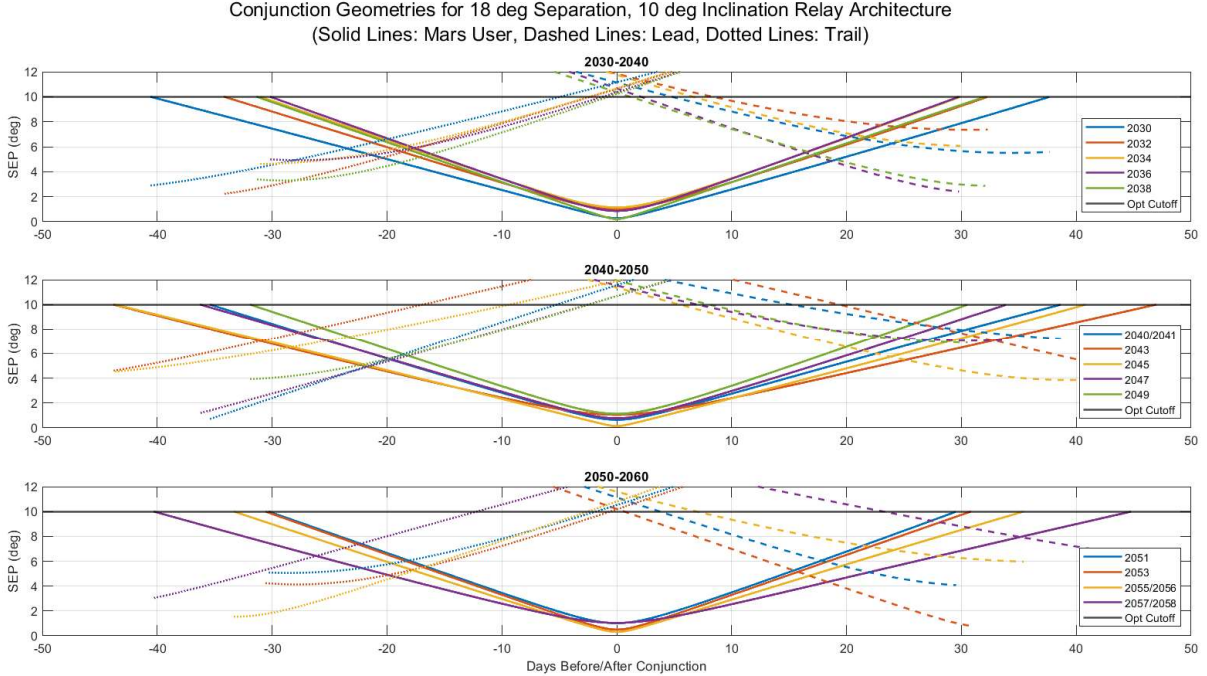


Figure 8. Conjunction geometries from 2030-2060 for the optimal relay geometry (18° relay separation angle, 10° relay inclination angle). Continuity of coverage is made visible in this plot.

a given navigating user. In either case, impulsive or low thrust maneuvers could be used to perform the necessary phase and inclination changes. Thus, during times when the geometry of the architecture is not constrained by the SEP/SPE angle requirements of conjunction and opposition ($\sim 90\%$ of the synodic period), strategic propulsive maneuvers can allow the relay architecture to better serve the instantaneous needs of its users.

V. Optical Communication with Mars Users

A. PPM Signal Format and Link Analysis

The Deep Space Relay architecture will utilize optical frequencies for downlink communication due to the significant data rate advantage they provide over RF. This improvement is primarily a result of the much higher frequency of optical signals compared to RF [13]. Higher frequency signals experience less beam divergence, allowing them to deliver more power to a receiving telescope of a given area, thus producing higher signal to noise ratios which in turn enable higher data rates.

Over a range of target data rates and background noise levels, the most power efficient and practically implementable method for modulation of an optical signal is intensity modulation at low duty cycles with photon-counting detectors. This modulation scheme may be modeled as a Poisson channel, and thus its performance can be described with analytical Poisson channel capacity models that have been developed in the literature. An optical signal can be detected either by coherent methods, which utilize the signal's phase information, or non-coherent methods (i.e., direct detection), which measure only the energy of the photons that strike the receiving photodetector [14]. This paper focuses on direct detection because it is the most power efficient method, and thus the most suitable for deep space applications [15].

Photon-counting detectors (which can detect the arrival of individual photons) enable the use of digital intensity modulation techniques. The simplest form of digital intensity modulation is binary on-off keying (OOK), in which each modulated bit consists of either an on or off pulse. Thus, the laser is always either "on" or "off" during a given time slot. A more complex direct detection modulation scheme is pulse position modulation (PPM). The PPM scheme

involves the transmission of successive message frames divided into M (i.e., the PPM modulation order) slots, with each slot having a duration of T_s seconds, resulting in frames of length MT_s . For each frame, a pulse is placed in one of the M slots in order to transmit $\log_2 M$ bits in that frame. Thus, the theoretical limit on the data rate for a given PPM scheme can be expressed with the following equation.

$$C_{PPM,lim} = \frac{\log_2(M)}{MT_s} \text{ bits/sec} \quad (1)$$

PPM is a near optimal modulation scheme for photon counting channels operating with a low duty-cycle (i.e., the laser is turned on a low percentage of the time) [15]. Equation 1 represents an idealized capacity for the optical link, however, the optimal PPM order M may vary depending on the received signal power and noise power at a given time, the data rate is not always strictly increasing with M . The detector pulse width and receiver bandwidth place a constraint on the optical link's minimum supportable slot width T_s , which is analogous to the bandwidth limit in the RF case. The minimum T_s , and thus the data rate supportable by the PPM link, is typically limited by the maximum processing speed of the transmitter and receiver, the laser pulse width, and the receiver clock accuracy.

One key objective of this paper is to investigate the deep space relay configuration that best improves the data return of optical communications with Mars users. In order to perform high level trade-offs between different relay configurations and facilitate evaluation of first order geometrical effects on link performance, an approximate optical PPM link capacity model was used [16] [17]. This model abstracts out some of the low-level details of a more complete link budget in favor of analytical tractability and implementation simplicity. The equations needed for this paper's optical Poisson PPM channel capacity simulation are developed below.

B. Received Signal Power

The first step in the optical link modeling process is to model the received signal power (P_r) at the focal plane of the receiving photodetector. An equation for the received power is given below.

$$P_r = P_t * G_t * G_r * L_s * L_a * \eta_t * \eta_r * \eta_{det} (W) \quad (2)$$

Where P_t is transmit power, G_t is transmit telescope gain, G_r is receive telescope gain, L_s is free space loss, L_a is atmospheric loss (i.e., atmospheric transmittance), η_t is transmitter efficiency, η_r is receiver efficiency, and η_{det} is detector quantum efficiency (which accounts for the probability that an incident photon is detected), all on a linear scale. In this formulation, losses that are physically unavoidable are accounted for as losses, while losses that could be recovered with a perfect hardware implementation are accounted for as efficiencies [17].

The free space loss as the signal propagates from transmitter to receiver is given by the following classic equation. Note that this formulation gives the free space loss on a linear scale and results in a positive $L_s \ll 1$.

$$L_s = \left(\frac{\lambda}{4\pi R} \right)^2 \text{ (linear)} \quad (3)$$

Where λ is the carrier wavelength of the optical signal and R is the range between the transmitting and receiving telescopes. The transmit telescope gain is given by the following equations [18].

$$G_t = \left(\frac{\pi * D_t}{\lambda} \right)^2 * \frac{2}{\alpha_t^2} * \left(e^{-\alpha_t^2} - e^{-\alpha_t^2 \gamma_t^2} \right)^2 \text{ (linear)} \quad (4)$$

$$\gamma_t = \frac{B_t}{D_t} \quad (5)$$

Where D_t is the transmit telescope primary aperture diameter, B_t is the transmit telescope secondary aperture diameter, γ_t is the transmit obscuration ratio, and α_t is the aperture to beamwidth ratio. The approximately optimal aperture to beamwidth ratio of $\alpha_t = 1.12$ will be used in this link model [18]. The receive telescope gain is given by the following equations [18].

$$G_r = \left(\frac{\pi * D_r}{\lambda} \right)^2 * (1 - \gamma_r^2) \text{ (linear)} \quad (6)$$

$$\gamma_r = \frac{B_r}{D_r} \quad (7)$$

Where D_r is the receive telescope primary aperture diameter, B_r is the receive telescope secondary aperture diameter, and γ_r is the receive obscuration ratio. For both the receive and transmit telescope cases, an idealized assumption will be made that the secondary aperture diameter is negligibly small.

Similar to the RF case, the optical signal is attenuated as it passes through an atmosphere. The optical frequency atmospheric transmittance (L_a) determines how much the signal is attenuated. Atmospheric transmittance values were obtained for a variety of weather conditions at each DSN location using a simulated data set produced with JPL's Strategic Optical Link Tool (SOLT). Atmospheric transmittance values for Mars were derived from [19]. In both the Earth and Mars cases, the atmospheric transmittance is interpolated from their respective data sets as a function of the receiving telescope elevation angle.

The transmitter efficiency (η_t) and receiver efficiency (η_r) account for the various losses that occur in the transmitting and receiving hardware respectively. Based on the capabilities of existing hardware, the transmit and receive efficiencies are assumed to be $\eta_t = 0.7$ and $\eta_r = 0.39$ respectively [17].

C. Detected Signal Power

Depending on the signal-to-noise-ratio (SNR) in the optical channel, it can be advantageous to restrict the detector's field of view (FOV) using an iris. Restricting the FOV filters out both noise and signal power, so an optimal balance must be reached depending on the SNR. As the SNR increases, the iris should be opened to encircle more of the signal power, thus the optimal iris opening size depends on the SNR at a given time. It has been shown that encircling 91.3% of the signal spot on the detector minimizes the worst-case loss due to using a suboptimal FOV for the instantaneous SNR [20]. This percentage can be mapped to an effective detector radius (δ) using the following process. First, the signal spot size (σ) on the photodetector of the receiver is calculated according to the following equation.

$$\sigma = (0.42\lambda F_r) \sqrt{\left(\frac{1}{r_0}\right)^2 + \left(\frac{1}{D_r}\right)^2} \quad (8)$$

The signal spot size depends on the size of the receiving telescope (focal length (F_r) and diameter (D_r)), the signal wavelength (λ), and most importantly the atmospheric coherence length/Fried parameter (r_0), which varies based on assumptions about the turbulence of the signal path medium. Next, the detector width (δ) which encircles a semi-optimal amount of the signal spot is calculated with the following equation.

$$\delta^2 = 4.88\sigma^2 \quad (9)$$

This detector width is "semi-optimal" in that it is the detector width which minimizes the worst-case loss due to mismatch between the actual FOV and the optimal FOV for the instantaneous SNR [20]. Finally, the worst-case loss-minimizing detector FOV (Ω_{det}) is calculated with the following equation (which assumes small angles):

$$\Omega_{det} = \pi \left(\frac{\delta^2}{F_r^2} \right) \quad (10)$$

Having defined the assumptions for the detector FOV, the detected signal power (P_d) can be calculated based on the received signal power (P_r) at the detector plane and the amount of the signal spot size encircled by the detector's iris using the following equation.

$$P_d = P_r \left(1 - e^{\left(\frac{-\delta^2}{2\sigma^2}\right)} \right) \quad (11)$$

D. Noise Power

The noise power sources accounted for in this optical link model are incident background light on the receiver aperture and dark noise electrons generated by the receiving photodetector (i.e., false photon detections). The thermal noise associated with the receiver is accounted for in the receiver efficiency term. The dominant source of background light in links from the Mars user or the relay to an Earth station is the “sky” radiance, while the dominant source of background light in links from the Mars user to the relay is the Mars “upwelling” radiance. The “sky” radiance refers to the light from the Sun that is scattered by Earth’s atmosphere during the daytime. The “upwelling” radiance refers to the light from the Sun that is reflected off of Mars and is visible to a relay when the Mars user is present on the illuminated side of Mars. The noise power due to background light ($P_{n,back}$) is given by the following equation [15].

$$P_{n,sky} = I_b * \Delta_\lambda * \Omega_{det} * \left(\frac{\pi * D_r^2}{4} \right) * \eta_r * \eta_{det} * \eta_{pol} \quad (W) \quad (12)$$

Where I_b is the background light radiance (either from the sky radiance or upwelling radiance effect depending on the link), Δ_λ is the receiver bandpass filter wavelength bandwidth, and η_{pol} is the polarization rejection efficiency (which accounts for the inclusion of a polarization rejection filter).

The background light radiance depends on the link type, the link geometry, the receiving telescope location, and atmospheric conditions. Similar to the atmospheric transmittance, the sky radiance values for Earth station links are obtained from simulated data produced with the SOLT tool. The simulated sky radiance data is produced as a function of telescope elevation angle, telescope location (i.e., Goldstone, Canberra, or Madrid), weather conditions (i.e., clear, hazy, and hazy with clouds), and most importantly SEP angle. For each weather condition and telescope location, the SOLT sky radiance data is given as a function of discrete SEP and elevation angles. For a given Earth link, a check is first performed to see if the Sun is above the horizon for the given telescope location at that time step (i.e., the elevation angle of the Sun is larger than 0°). If the Sun is below the horizon of the receiving Earth telescope while the transmitting Mars user or relay is present in the sky, then the sky radiance term is set to zero. If the Sun is above the horizon of the receiving Earth telescope while the transmitting Mars user or relay is present in the sky, then the optical link model performs a 2-dimensional linear interpolation of the simulated radiance data for the SEP and elevation angles at the given time step. This interpolated sky spectral radiance value is then plugged into Equation 12 to calculate the background light noise power for the Earth link. A similar process is performed with the upwelling radiance data for relay links, which is obtained from [21]. This data is also provided as a function of telescope elevation angle and SEP angle. In this case, a check is first performed to determine if the Mars surface user transmitting to the relay is on the illuminated side of Mars. Alternatively, if the Mars user is an orbiter, a check is performed to determine if the receiving telescope’s FOV passes over the illuminated side of Mars. If these conditions are met, then the upwelling radiance value is interpolated from the data set and used in Equation 12 to calculate the background light noise power for the Mars link.

The noise power contribution from dark noise electrons can be calculated with the following equations [17].

$$P_{n,dark} = 4 * \delta^2 * l_d * E_\lambda \quad (13)$$

$$E_\lambda = \frac{h * c}{\lambda} \quad (14)$$

Where l_d is the detector dark rate (rate of false electron counts per unit area of the detector), h is Planck’s constant, c is the speed of light, and E_λ is the energy per photon. The background light noise power and dark noise power terms are then added together to compute the overall noise power (P_n).

$$P_n = P_{n,dark} + P_{n,sky} \quad (15)$$

E. PPM Channel Capacity

As previously mentioned, it is assumed that the optical link is pulse-position-modulated (PPM) with modulation order (i.e., number of slots) M and slot-widths of duration T_s . Additionally, it is assumed that the noise affecting the link follows a Poisson distribution. Using these assumptions and given that the detected signal power (P_d) and noise power (P_n) have been calculated as discussed above, the following equation can be used to calculate the Poisson PPM channel capacity (in bits/second) [17].

$$C_{PPM} = \frac{1}{E_\lambda \ln(2)} \left(\frac{P_d^2}{P_d \frac{1}{\ln(M)} + P_n \frac{2}{M-1} + P_d^2 \frac{MT_s}{\ln(M) E_\lambda}} \right) \text{ (b/s)} \quad (16)$$

Where P_d and P_n are in Watts.

In the capacity equation above, there are three distinct terms being added in the denominator, the first term being $P_d/\ln(M)$, the second being $2P_n/(M-1)$, and the third being $P_d^2 MT_s/(\ln(M) E_\lambda)$. Depending on which of these terms dominates, the optical link will be in one of three different operation regimes [16]. When the first term is much larger than the other two terms, the link operates in a high signal-to-noise ratio regime in which the capacity is approximated with Equation 17. In this regime, the capacity has the familiar inverse square relationship with the range between transmitter and receiver (R).

$$C_{PPM} \approx \frac{P_d \log_2(M)}{E_\lambda} \propto \frac{1}{R^2} \quad (17)$$

When the second term is much larger than the first and third terms, the link operates in a low signal-to-noise ratio regime in which the capacity is approximated with Equation 18. In this regime, the capacity falls off with R^4 .

$$C_{PPM} \approx \frac{P_d^2 (M-1)}{2P_n E_\lambda \ln(2)} \propto \frac{1}{R^4} \quad (18)$$

When the third term is much larger than the first and second terms, i.e., high average power mode, the link operates in a minimum slot-width constrained regime in which the capacity saturates at the theoretical PPM data rate limit.

$$C_{PPM} \approx \frac{\log_2(M)}{MT_s} \quad (19)$$

The regime of operation, and thus the range dependence of the optical link, is closely related to the SNR of the link. The transition between regimes/range dependencies occurs when the PPM channel transitions from a high SNR shot-noise dominated regime (i.e., receiver hardware noise is the dominant noise source) to a low SNR background noise dominated regime (i.e., background light from either sky radiance or upwelling radiance is the dominant noise source). This behavior of the optical link differs from the familiar behavior of a coherent RF channel, which is thermal noise limited and always goes as $1/R^2$.

For deep space optical communications with Mars users, the user spacecraft periodically enters solar conjunction, during which the line-of-sight from an Earth-based receiver to the Mars user is near the Sun, as quantified by a small SEP angle. During conjunction, the orbital geometry causes the Earth-Mars range to reach a maximum as the SEP angle reaches a minimum, thus the impact of solar conjunction on optical link performance is two-folds. First, the received signal will be at its minimum power due to the maximum range. Second, the background noise contribution from sky radiance increases significantly at small SEP angles. The combination of decreased signal power and increased noise power results in a low SNR, causing the link to switch from the signal dominant regime to the noise dominant regime where the capacity goes with $1/R^4$, resulting in a rapid decrease in data return performance as conjunction is neared, and eventually total link outage as the SEP angle dips below the 10° threshold.

On the other hand, during Mars opposition, the range to Mars is at a minimum and the Earth terminal is pointing at the night sky when tracking a Mars user, thus there is no sky radiance noise seen by the Earth receiver. However, the Mars user terminal pointing back towards Earth will see a low angular separation between the Earth and the Sun (low SPE angle). This small SPE angle can prohibit the spacecraft receiver from acquiring the uplink beacon from Earth, which is needed for proper pointing of the downlink signal. Given this combination of factors, the data return during opposition will be high up until the point that the SPE angle dips below the 3° threshold, at which point there will be a brief period of total link outage.

F. Optical Link Results

The optical link capacity model just described was combined with the relay geometry simulation discussed in Section IV to analyze the data return achievable for an equatorial Mars surface user of the relay architecture. The link and hardware assumptions made for this analysis are summarized in Table 2 in the Appendix. The data return performance of the DWE downlink between the Mars surface user and the DSN was analyzed first, as this would serve as a baseline to evaluate the performance of the relay architecture. It should be noted that at each simulation time step, the DSN location (i.e., Goldstone, Canberra, or Madrid) providing the best visibility to the Mars user was the one used for the calculation of the optical channel capacity. Thus, these results assume continuous devotion of DSN resources to the Mars user, and therefore serve as an upper limit for achievable data return to Earth. Furthermore, this optical link model ignores many lower level details of the optical link, as it is intended to simply capture the first order effects of the link geometry on communication performance. It quantifies the communication performance using the approximate channel capacity, which is a theoretical upper limit on the channel's performance. Additionally, it is assumed for simplicity that all links use a fixed PPM order, rather than a PPM order optimized for the instantaneous SNR of the link. Given these approximations and simplifications, the specific data return values shown are less important than the overall trends in data return. Figures 9 and 10 depict the DWE link communication performance using the metrics of link access time and data return per day respectively.

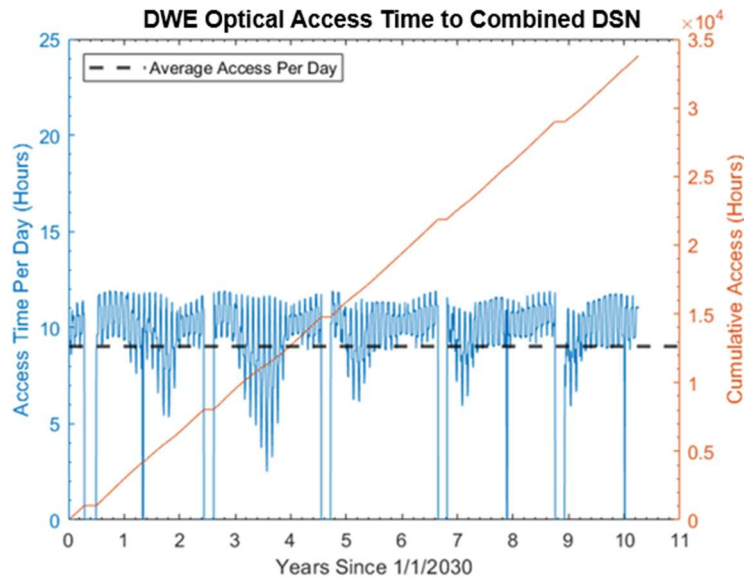


Figure 9. DWE optical downlink access time for an equatorial Mars surface user.

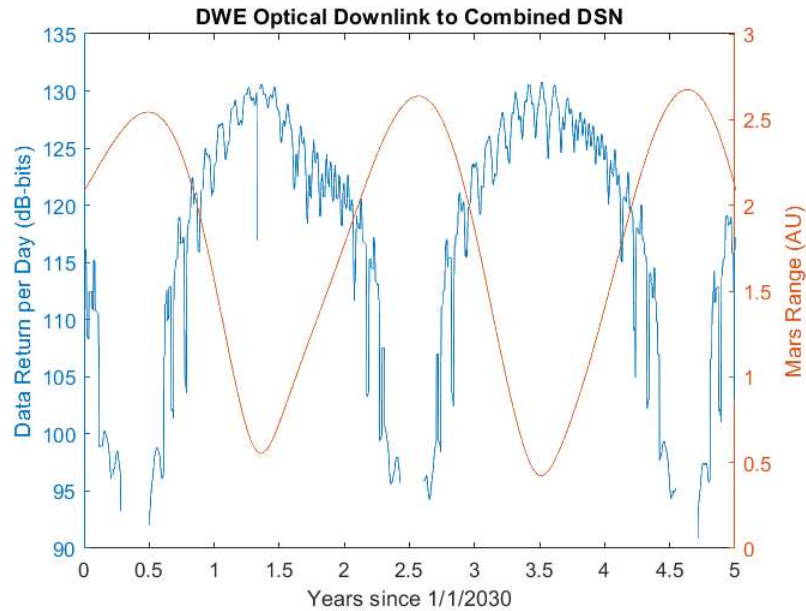


Figure 10. DWE optical downlink data return per day for an equatorial Mars surface user.

Figure 9 shows that the DWE downlink is accessible for about 10-12 hours on most days during the 2030-2060 time period. This is due to the fact that the Mars user is located on the Mars surface and rotates out of view from Earth for about half of each Earth day. Additionally, there are elevation angle masks of 20° assumed for each DSN station to account for local topography and the difficulty of optical signal detection when there is a long signal path through atmosphere. This further cuts into the access time for the DWE downlink. The access time drops to zero during each conjunction period and during some of the opposition periods. In Figure 10, it can be seen that the data return per day drops off sharply as Mars nears conjunction. This is due to the link moving from the signal power dominated regime to the noise power dominated regime as the solar background noise increases. At conjunction there is no data return. This is due to the outages caused by the Sun-Earth-Mars angle falling below the optical threshold.

Daily fluctuations in the data return can also be seen. These daily fluctuations are larger near conjunction and smaller near opposition. This behavior is due to the synodic variation in the amount of time per day that both the Sun and Mars are present in the sky of a particular DSN station. This balance between daytime viewing opportunities (when Mars and the Sun are both present above the horizon) and nighttime viewing opportunities (when Mars is present in the sky, but the Sun is below the horizon) varies over the course of the Earth-Mars synodic period and depends on the latitude of the DSN station, as shown in Figure 11 (next page). Near conjunction, communication with the Mars user occurs predominantly in the daytime, resulting in solar noise degradation of the link for the majority of a day's tracking pass. This serves as a third limitation of link performance near conjunction, in addition to the range and SEP challenges. Near opposition, communication with Mars users occurs predominantly during the nighttime, meaning that solar noise degrades the link for only a small portion of the tracking pass.

Next, the communication performance for the full relay architecture was analyzed assuming the optimal geometry of 18° relay separation angles and $\pm 10^\circ$ inclination angles for the leading and trailing relays respectively. The communication benefit of the relay architecture from an access time perspective is depicted in Figure 12. In this figure, it can be seen that the combined leading/trailing relay architecture provides about 10 hours per day of additional access time compare to the DWE link alone. This is due to the fact that as the Mars surface user rotates out of view of the Earth, it will still be visible to the lead relay. Then, as the surface user rotates out of view of the lead relay, it will rotate into view of the trailing relay before becoming visible to the Earth. There are also large spikes in the additional access time corresponding to the points during conjunction and opposition periods where both the lead and trail relays are above the SEP/SPE angle constraints, but the DWE link is not. With the full architecture (i.e., the combination of Earth stations and leading and trailing relays), there is an average of about 20 hours of access time per day for an equatorial Mars surface user, with many days experiencing a full 24 hours of access.

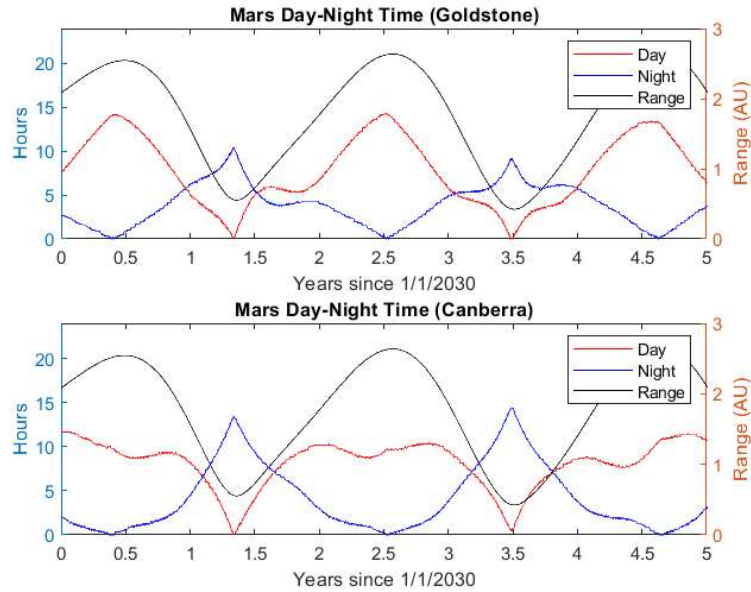


Figure 11. Mars daytime/nighttime geometry.

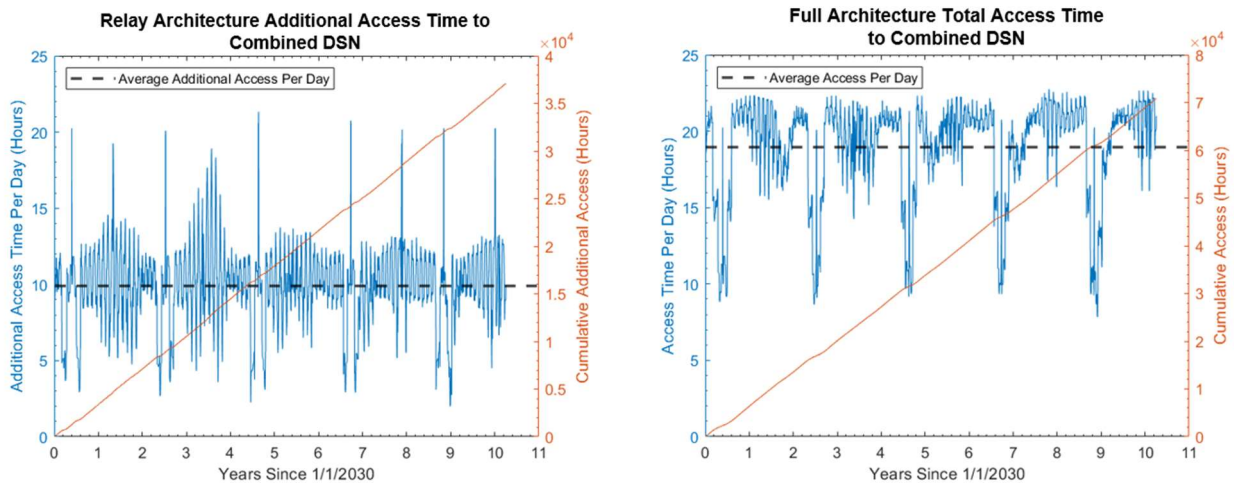


Figure 12. Additional access time provided by combined leading/trailing relay architecture to the equatorial Mars surface user (left). Total access time to Earth via full architecture (relays and Earth stations) for the equatorial Mars surface user (right).

The communication benefit of the relay architecture from a data return perspective is depicted in Figure 13 (next page), which shows the maximum data return per day achievable for the DWE link (blue), the relay links (red), and the combined architecture link (yellow). For the lead relay link, the data return was limited by the smaller of the capacities achievable for the Mars-relay hop and the relay-Earth hop. The relay-Earth hop capacity was computed using whichever DSN had the best visibility to the relay at a given time, as was done in the DWE case. This same process was performed to calculate the date return for the trail relay link. Then, the overall relay link data return was calculated by integrating the larger of the capacities achievable through using the leading or trailing relay links over

each time step. Finally, the combined relay architecture downlink data return was computed by integrating the best link capacity between either the direct link, the lead relay link, or the trail relay link over each time step.

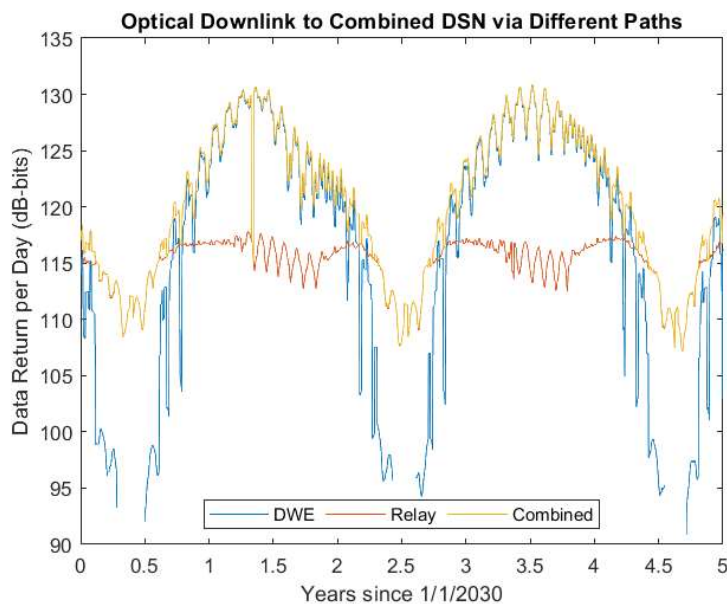


Figure 13. Maximum optical downlink data return per day for direct, relay, and combined architecture links.

The communication benefit of the relay architecture is demonstrated in Figure 13 by the time periods in which the relay link outperforms the DWE link. This occurs not only during complete outages, but also in the months leading up to and after each conjunction period. It can also be seen that the relay links are limited by the capacity of the Mars user-relay hop for the majority of the synodic period, however when the relays near their conjunctions, the proximity hop briefly outperforms the relay-Earth hop. The combined relay architecture results in continuous coverage over the entire time interval and additional data return per day on every day of the interval, with particularly large advantages during Mars conjunction. These communication advantages are due to a combination of the additional coverage time enabled by the relays seeing the Mars user when it is occulted from the DSN each day and the higher SEP angles that the link geometry enables near or at conjunction.

VI. Deep Space Trilateration Concept

The unique placement of the relay spacecraft in inclined, Mars leading and trailing orbits creates an opportunity for them to serve as deep space navigation beacons. The relay architecture can provide range and Doppler measurements that provide navigation services to users in the Mars vicinity and in the inner-planets space volume. The Deep Space Relay Architecture will provide navigation to two different service volumes using two different navigation schemes. The first service volume would be made up of users in the Mars vicinity (i.e., Mars surface users and orbiters), which will have access to both relays and the Earth for range measurements. These range measurements will be used in the trilateration positioning scheme discussed in this section. The second service volume is for spacecraft within the inner planets region (i.e., below Mars level orbit). This service volume would still be receiving range and doppler measurements from the Earth and relays, but with the Earth serving as a reference station. Navigation for this service volume through a Joint Doppler and Ranging scheme (JDR). A detailed discussion of this scheme is outside of the scope of this paper but is provided in a companion paper [10].

The traditional trilateration method used by GNSS systems positions a user via range measurements from at least 3 navigation nodes whose positions are well known. In the deep space trilateration case proposed for the minimal relay architecture, a user in the vicinity of Mars receives range measurements from three geometrically dispersed locations:

one from the leading relay, one from the trailing relay, and one from a DSN station on Earth. The two relays are in orbits inclined with respect to the ecliptic plane (one below and one above the plane), thus providing good geometric diversity in the out-of-ecliptic-plane direction. This analysis assumes that the Mars user knows the ephemeris of the relay orbiters and the Earth to high precision, which could be accomplished by each relay and station broadcasting their ephemeris as part of the ranging signal. With GNSS trilateration, a position fix requires a minimum of four range measurements due to the need for the user spacecraft to estimate a clock bias. However, due to the limited navigation nodes in the leading/trailing relay architecture, this analysis assumes the use of two-way range measurements in order to remove the need to estimate a clock bias. the navigation method used for users within the Mars vicinity. This service volume includes users on the surface of Mars, in low Martian orbit, and up to high Martian orbit.

A. Dilution of Precision Analysis

To analyze the performance of the trilateration scheme for navigating Mars users, a dilution of precision (DOP) analysis is performed. This analysis begins with the definition of a range measurement model.

$$\rho_i = G_i(\vec{x}_M) = \sqrt{(x_M - x_{Ni})^2 + (y_M - y_{Ni})^2 + (z_M - z_{Ni})^2} \quad (20)$$

$$i = \begin{cases} E \text{ (Earth)} \\ L \text{ (Lead relay)} \\ T \text{ (Trail relay)} \end{cases} \quad (21)$$

Where \vec{x}_M is the cartesian position vector of the Mars user, i denotes the navigation node providing the range measurement, and $[x_i, y_i, z_i]^T$ defines each navigation node's position.

The range measurement model is nonlinear in the parameters to be estimated (i.e., the cartesian coordinates of the position vector), thus a linearized approach will be used to solve for the estimated position vector. The linearized measurement model (\vec{y}) is obtained by taking the Jacobian of the range measurement model in Equation 20.

$$\vec{y} = \begin{bmatrix} y_E \\ y_L \\ y_T \end{bmatrix} = H\vec{x}_M + \vec{\varepsilon} \quad (22)$$

$$H = \frac{\partial G_i(\vec{x}_M)}{\partial \vec{x}_M} = \begin{bmatrix} \frac{\partial G_E}{\partial x_M} & \frac{\partial G_E}{\partial y_M} & \frac{\partial G_E}{\partial z_M} \\ \frac{\partial G_L}{\partial x_M} & \frac{\partial G_L}{\partial y_M} & \frac{\partial G_L}{\partial z_M} \\ \frac{\partial G_T}{\partial x_M} & \frac{\partial G_T}{\partial y_M} & \frac{\partial G_T}{\partial z_M} \end{bmatrix} = \begin{bmatrix} \frac{x_M - x_E}{\rho_E} & \frac{y_M - y_E}{\rho_E} & \frac{z_M - z_E}{\rho_E} \\ \frac{x_M - x_L}{\rho_L} & \frac{y_M - y_L}{\rho_L} & \frac{z_M - z_L}{\rho_L} \\ \frac{x_M - x_T}{\rho_T} & \frac{y_M - y_T}{\rho_T} & \frac{z_M - z_T}{\rho_T} \end{bmatrix} \quad (23)$$

$$\vec{\varepsilon} = \begin{bmatrix} \varepsilon_E \\ \varepsilon_L \\ \varepsilon_T \end{bmatrix}, \quad E[\vec{\varepsilon}] = 0, \quad Cov[\varepsilon\varepsilon^T] = R = \begin{bmatrix} \sigma_E^2 & 0 & 0 \\ 0 & \sigma_L^2 & 0 \\ 0 & 0 & \sigma_T^2 \end{bmatrix} \quad (24)$$

Where H is the Jacobian of the range measurement model and $\vec{\varepsilon}$ are the measurement errors, which are assumed to be zero mean and uncorrelated with covariance R .

The purpose of the DOP analysis is to assess the navigation potential of the relay architecture from a purely geometrical point of view. In other words, this analysis is intended to assess the quality of the geometry of the minimal relay architecture for navigating various Mars vicinity users. Thus, the covariance for a Mars user position estimate will be derived assuming that the range measurements from each station have an error of $\sigma_\rho = 1 \text{ m}$.

$$\sigma_E = \sigma_L = \sigma_T = \sigma_M = \sigma_\rho = 1 \text{ m} \quad (25)$$

$$R = \begin{bmatrix} \sigma_E^2 & 0 & 0 \\ 0 & \sigma_L^2 & 0 \\ 0 & 0 & \sigma_T^2 \end{bmatrix} = \begin{bmatrix} \sigma_\rho^2 & 0 & 0 \\ 0 & \sigma_\rho^2 & 0 \\ 0 & 0 & \sigma_\rho^2 \end{bmatrix} = I_{3 \times 3} \sigma_\rho^2 \quad (26)$$

The covariance of the position estimate error (i.e., $\vec{x}_M - \hat{x}_M$ where \vec{x}_M is the true Mars user position and \hat{x}_M is the estimated position) for an estimate made with this linearized range measurement model is given by the following equation [8].

$$P = E[(\vec{x}_M - \hat{x}_M)(\vec{x}_M - \hat{x}_M)^T] = (H^T R^{-1} H)^{-1} = (H^T H)^{-1} \sigma_\rho^2 \quad (27)$$

$$P = \begin{bmatrix} \sigma_x^2 & \sigma_x \sigma_y & \sigma_x \sigma_z \\ \sigma_x \sigma_y & \sigma_y^2 & \sigma_y \sigma_z \\ \sigma_x \sigma_z & \sigma_y \sigma_z & \sigma_z^2 \end{bmatrix} \quad (28)$$

The covariance matrix P is made up of the variances of the estimation errors in each cartesian direction (σ_x^2 , σ_y^2 , and σ_z^2), as well as the covariance of the estimation errors between cartesian directions ($\sigma_x \sigma_y$, $\sigma_x \sigma_z$, and $\sigma_y \sigma_z$). The diagonal components of the covariance matrix P will be used as metrics for navigation performance. Specifically, the standard deviation of the estimation errors in each coordinate direction (σ_x , σ_y , and σ_z) correspond to the geometric dilution of precision along each coordinate direction and the root sum square of these standard deviations corresponds to the 3D geometric DOP (σ_{xyz}).

$$\sigma_{xyz} = \sqrt{\sigma_x^2 + \sigma_y^2 + \sigma_z^2} \quad (29)$$

The geometric DOP was computed for the full analysis period to assess the navigation quality of the relay geometry. The Jacobian matrix H was evaluated by plugging in the simulated inertial coordinates of the Mars user and each measurement station, as well as the true simulated ranges between them (with no noise added), at each valid time step (t_v). By using the true values of the position vectors and ranges, this analysis isolates the quality of the relay architecture's geometry for positioning a given Mars user. The geometric DOP in each coordinate direction as well as the 3D DOP is given in Figure 14 for an equatorial Mars surface user. This plot assumes continuous access of the user to Earth stations, the lead relay, and the trail relay. This is not a realistic assumption, but it is made here for the purposes of isolating the quality of the navigation geometry.

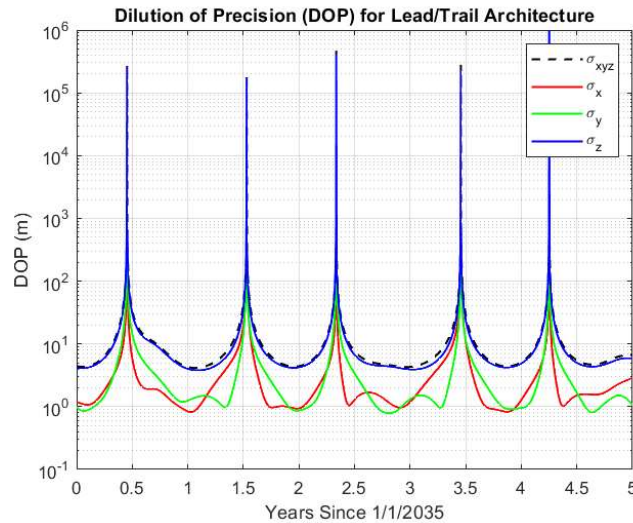


Figure 14. DOP for Mars equatorial surface user.

Although the inclined relay orbits aid in improving the z-axis (i.e., out of ecliptic plane) geometry, poor positioning performance along the z-axis is still the limiting factor in this architecture. As shown in Figure 14, the total 3D position error σ_{xyz} is heavily dependent on σ_z , while both σ_x and σ_y are significantly more accurate. Additionally, there are moments throughout the analysis period with divergent spikes. These spikes align with the times that the user intersects the plane made by the two relays and Earth (Figure 15). When the user is on this plane, the measurements provide no information about the direction out of the Earth-relay plane, leading to a near-singular Jacobian matrix and thus poor DOP.

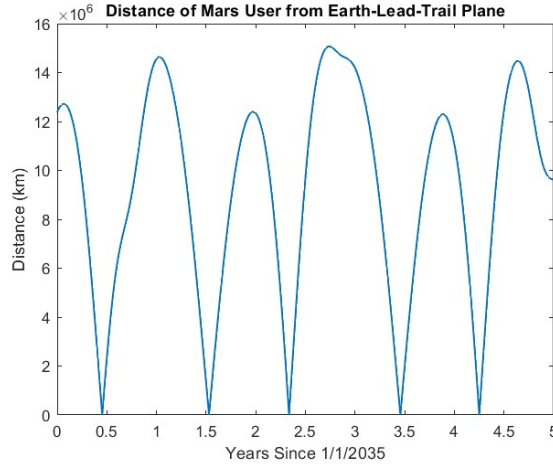


Figure 15. Mars user distance from the Earth-relay plane.

These intersections with the Earth-relay plane lead to short intervals in time with high error. To analyze how much of the analysis interval has undesirable navigation performance, the DOP's at each time step were grouped into bins based on their severity, as is shown in Figure 16. This analysis demonstrates that over the course of the five-year interval from 2035-2040, the total DOP is greater than 100 meters (i.e., extremely poor) only 4.4% of the time. The total DOP is under 10 m (i.e., excellent) 69.6% of the time, and under 100 m (i.e., fair) for 95.6% of the interval. Thus, the geometry of the relay architecture is suitable for trilateration of Mars users from a DOP perspective.

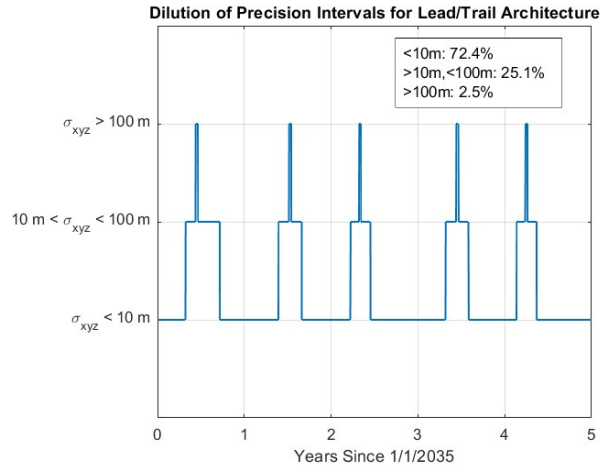


Figure 16. Intervals of 3D DOP being below 10 m, below 100 m, and above 100 m for an equatorial Mars surface user.

B. Expanding the Relay Architecture

The DOP analysis just discussed assumed continuous access to all 3 nodes of the leading/trailing architecture for the purposes of assessing just the navigation geometry quality of the architecture for Mars users, which is high for the majority of the analysis period. However, a consideration of access to range measurements at each time step for Mars surface users highlights a flaw in the minimal leading/trailing relay architecture. This flaw is that in order to collect 3 measurements at the same time and thus enable the trilateration scheme, the lead relay, trail relay, and an Earth station must all have access to the Mars user simultaneously, which depending on the nature of the Mars user, may not happen very often. For an orbiting user in a high Mars orbit (i.e., 6000 km altitude) 3 range measurements are available simultaneously from the minimal relay architecture for ~80% of the analysis period. For an orbiting user in a low Mars orbit (i.e., 300 km altitude) 3 range measurements are available simultaneously for only ~26% of the analysis period. For an equatorial Mars surface user, 3 range measurements are available simultaneously for only ~3% of the analysis period, and this number gets even lower as the surface user rises in latitude. The availability of different numbers of range measurements to an equatorial Mars surface user is shown in Figure 17.

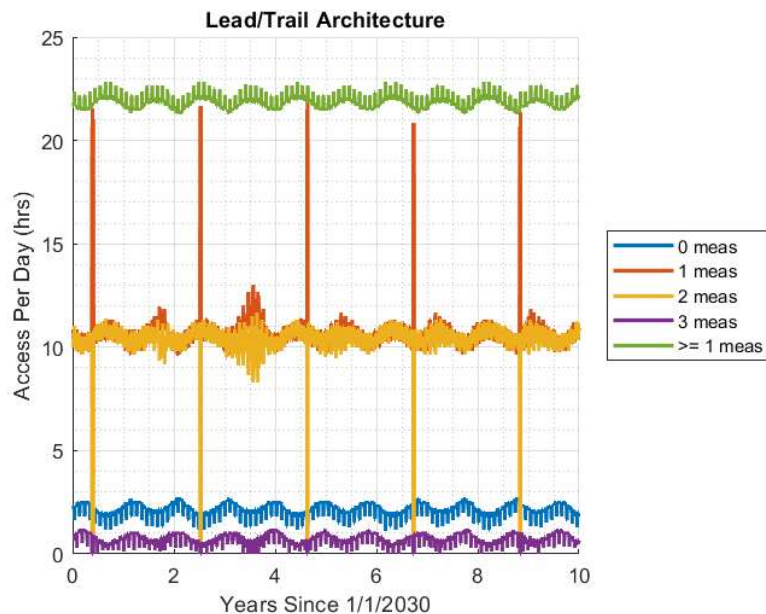


Figure 17. Simultaneous availability of range measurements to an equatorial Mars surface user from the minimal relay architecture .

This is clearly a shortcoming for the trilateration scheme if it can only be realized a small percentage of the time. In order to combat this problem of lack of access to 3+ range measurements, an expanded relay architecture is being analyzed which would add one more relay to the existing leading/trailing architecture. The current orbits of interest for this third relay are Mars L2 halo orbits. The expanded relay architecture involving halo orbits is the focus of work that is currently in progress and thus will not be discussed in detail in this paper. However, the benefits of using a halo relay in an expanded Deep Space Relay architecture are summarized below.

1. The addition of a third relay results in 4 total navigation nodes in the architecture, thus enabling the one-way ranging scheme discussed in Section III.
2. The addition of a third relay will provide more opportunities for Mars users to have access to 3 simultaneous range measurements.
3. The placement of the third relay in an L2 Halo orbit will improve the geometric DOP of the relay geometry.

4. The placement of the third relay in an L2 Halo orbit (i.e., on the back side of Mars relative to Earth) will provide additional coverage time for all Mars users, particularly for Mars surface users at higher latitudes, which are poorly covered by the minimal relay architecture.
5. The placement of the third relay in an L2 Halo orbit means it will be much closer to Mars users than the leading and trailing relays. Thus, smaller Mars users will often receive a data return advantage by making the short hop to the halo relay, which will then forward the signal to Earth. This advantage would persist even when Mars is not in conjunction.

VII. Conclusion

This paper presented a minimal Deep Space Relay architecture with two orbiters; one in a leading orbit inclined with respect to the Mars orbital plane and one in a trailing orbit inclined in the opposite direction with respect to the Mars orbital plane. Under the right conditions, this architecture could be made to solve the Mars conjunction communication problem for optical links and provide navigation services to spacecraft in the Mars vicinity and the inner planets space volume. It was found that an architecture with relay separation angles of 18° and inclination angles of $\pm 10^\circ$ is optimal for the relay's combined communication and navigation providing roles.

For communication, this combination of relay separation and inclination angles guarantees a link whose SEP and SPE angles exceed the optical thresholds at all times, thus eliminating link outages during conjunction and opposition. This geometry also strikes an optimal balance between low proximity link ranges (which minimizes the telecom burden on Mars users) and sufficiently high relay SEP angles (which keeps the optical relay links out of the noise dominated regime). The net results of these communication factors are continuous Mars coverage and significantly improved Mars data return during the 2030-2060 time period.

The optimal relay geometry identified for communication also enables navigation for deep space users. Two navigation schemes can be implemented for two different potential users of the relay network: a trilateration scheme that can be used to navigate spacecraft in the Mars vicinity and a DD-JDR scheme that can be used to navigate users within Earth's orbit. The placement of the relays in heliocentric, inclined, Mars leading/trailing orbits results in diverse measurement geometry, which in turn enables geometric DOP of better than 100 meters for $\sim 95\%$ of the analysis period, and better than 10 meters for $\sim 70\%$. This initial navigation analysis shows that the relay architecture provides sufficient navigation geometry for deep space applications. Further analyses will more thoroughly quantify the navigation performance of both navigation schemes and their respective service volumes using more realistic measurement models and filter based methods.

An expansion of the minimal architecture with an additional relay orbiter placed in an L2 halo orbit is currently being studied. This expanded architecture would yield both communication and navigation benefits. For communication, this halo relay would provide additional coverage times for all users and would partially or fully eliminate the proximity link data return bottle neck. For navigation, the expanded halo relay architecture would provide more opportunities for Mars users to receive 3 simultaneous range measurements, thus allowing trilateration to be performed more frequently. It also makes it possible for certain Mars users to receive 4 simultaneous range measurements, which enables the use of the more operationally flexible one-way ranging scheme and pushes the navigating user closer to real-time positioning capability.

VIII. Appendix

Table 2. Optical Link Parameters

| Link Parameters | | | |
|---|---|-------------------------|---------------------------------|
| | Parameter | Value | [Source] / Note (see next page) |
| Signal Parameters | PPM Modulation Order, M | 32 | [17] |
| | Slot Width, T_s | 0.5 ns | [17] |
| Path Parameters | Fried Parameter, r_0 (for Relay-Earth links) | 5 cm | SOLT Data |
| | Fried Parameter, r_0 (for DTE links) | 5 cm | SOLT Data |
| | Fried Parameter, r_0 (for Mars Surface User-Relay links) | 47 cm | SOLT Data |
| | Fried Parameter, r_0 (for Mars Orbiting User-Relay links) | 3e7 cm | SOLT Data |
| | Atmospheric Transmittance (Earth) | 0.8405 – 0.9069 | SOLT Data |
| | Atmospheric Transmittance (Mars) | 0.05 – 0.7 | [19] |
| Earth Station Parameters | | | |
| | Parameter | Value | [Source] / Note (see next page) |
| Optical Receive Parameters | Wavelength, λ | 1.550 μm | [17] |
| | Receive Telescope Diameter, D_r | 8/10/12 m | [17] |
| | Receive Telescope Focal Length, F_r | 16/20/24 m | [17] |
| | Bandpass Filter Bandwidth, Δ_λ | 2e-4 μm | [17] |
| | Detector Radius, δ | 0.46/0.58/0.69 mm | [20] |
| | Detector Field of View, Ω_{det} | 2.6/2.6/2.6 nsr | [20] |
| | Dark Electron Rate, I_d | 1e6 e/s/mm ² | [17] |
| | Receiver Efficiency, η_r | 0.39 | [17] |
| | Detector Quantum Efficiency, η_{det} | 0.4 | [17] |
| Polarization Rejection Efficiency, η_{pol} | 0.5 | [17] | |
| Relay Parameters | | | |
| | Parameter | Value | |
| Optical Receive Parameters | Wavelength, λ | 1.550 μm | [17] |
| | Receive Telescope Diameter, D_r | 50 cm | [17] |
| | Receive Telescope Focal Length, F_r | 1 m | [17] |
| | Bandpass Filter Bandwidth, Δ_λ | 2e-4 μm | [17] |
| | Surface User Detector Radius, δ | 4.20 μm | [20] |
| | Surface User Detector Field of View, Ω_{det} | 0.0554 nsr | [20] |
| | Orbiting User Detector Radius, δ | 2.88 μm | [20] |
| | Orbiting User Detector Field of View, Ω_{det} | 0.0260 nsr | [20] |
| | Dark Electron Rate, I_d | 1e6 e/s/mm ² | [17] |
| | Receiver Efficiency, η_r | 0.39 | [17] |
| | Detector Quantum Efficiency, η_{det} | 0.4 | [17] |
| | Polarization Rejection Efficiency, η_{pol} | 0.5 | [17] |
| Optical Transmit Parameters | Wavelength, λ | 1.550 μm | [17] |
| | Transmit Telescope Diameter, D_t | 50 cm | [17] |
| | Transmit Power, P_t | 17 W | [17] |
| | Transmitter Efficiency, η_t | 0.7 | [17] |
| Mars User Parameters | | | |
| | Parameter | Value | |
| Optical Transmit Parameters | Wavelength, λ | 1.550 μm | [17] |
| | Transmit Telescope Diameter, D_t | 22 cm | [17] |
| | Transmit Power, P_t | 4 W | [17] |
| | Transmitter Efficiency, η_t | 0.7 | [17] |

IX. Acknowledgements

I would like to acknowledge the people at JPL and SSDL who I worked with on this project. To Dr. Kar-Ming Cheung, thank you for entrusting me with this fascinating study and for your mentorship over the past two years, I've learned so much about deep space telecommunications by working with you and I'm excited to continue working in your group at JPL full time. To Dr. Hua Xie and Dr. Charles Lee, thank you for the contributions you made to the optical link model and relay geometry simulation aspects of this study respectively, I could not have gotten these results without you. To William Jun, thank you for the expertise you've shared with me on navigation topics both during this project and throughout my years in SSDL. In my first weeks of joining the lab, you patiently explained the workings of GPS to me and sparked my initial interest in navigation architectures, so I would not be where I am today without your mentorship. Finally, to my research advisor Dr. Glenn Lightsey, thank you for both a fantastic undergraduate and graduate research experience. My time in your lab has been the most rewarding part of my academic life at Georgia Tech and the doors it has opened have gotten me to exactly where I want to be professionally.

This research was carried out with funding from the Jet Propulsion Laboratory, under a contract with the National Aeronautics and Space Administration (80NM0018D0004).

References

- [1] C. Thornton, J. Border, "Radiometric Tracking Techniques for Deep Space Navigation", *DESCANSO Book Series*, 2000.
- [2] Starship Users Guide, Rev 1.0, March 2020.
- [3] P. Lord, G. Ommering, "Evolved Commercial Solar Electric Propulsion: A Foundation for Major Space Exploration Missions", 31st Space Symposium, Colorado Springs, Colorado, April 2015.
- [4] T. Ely, E. Burt, J. Prestage, "Using the Deep Space Atomic Clock for Navigation and Science", IEEE Transactions on Ultrasonics, Ferroelectrics, and Frequency Control, June 2018.
- [5] J. Breidenthal, et. Al., "Deep Space Relay Terminals for Mars Superior Conjunction," SpaceOps Conference 2018, Marseille, France, May 2018.
- [6] D. Morabito and R. Hastrup, "Communications with Mars During Periods of Solar Conjunction: Initial Study Results", IPN Progress Report 42-147, 2001.
- [7] B. Moision, W. Farr, "Range Dependency of the Optical Communications Channel," Interplanetary Network Progress Report, 42-199, November 15, 2014.
- [8] P. Misra, P. Enge, "Global Positioning System: Signals, Measurements, and Performance," Revised 2nd Edition, Ganga-Jamuna Press, 2012.
- [9] W. Jun, K. Cheung, G. Lightsey, "Improved Surface Positioning with Measurement Differences in Joint Doppler and Ranging," IEEE Aerospace Conference 2023, Big Sky, Montana, March 2023.
- [10] K. Cheung, P. Carter, "Deep Space Relay Architecture for Communications and Navigation", IEEE Aerospace Conference 2023, Big Sky, Montana, March 2023.
- [11] M. Jesick, "Mars Trojan Orbits for Continuous Earth-Mars Communication", *J Astronaut Sci* 67, 902–931 (2020).
- [12] Joshua P. Davis, John P. Mayberry, and Jay P. Penn, "Cost Reductions and Fuel Efficiency: High-Power Solar Electric Propulsion in Space", *Game Changer*, Aerospace Corp.
- [13] S. Sburlan, "Introduction to Optical Communication for Satellites." Keck Institute for Space Studies Workshop, 2016.
- [14] S. Dolinar, et al. "Chapter 4: Optical Modulation and Coding." *Deep Space Optical Communications*, edited by: Hamid Hemmati, JPL DESCANSO Book Series, 2005.
- [15] S. Dolinar, et al. "Fundamentals of Free-Space Optical Communication." Keck Institute for Space Studies Workshop on Quantum Communication, Sensing and Measurement in Space, 2012.
- [16] B. Moision and H. Xie, "An Approximate Link Equation for the Direct-Detected Optical PPM Link", IPN Progress Report 42-199, 2014.
- [17] B. Moision, et. al., "An Optical Communications Link Design Tool for Long-Term Mission Planning for Deep-Space Missions"
- [18] B. Klein and J. Degnan, "Optical Antenna Gain 1: Transmitting Antennas," *Applied Optics*, vol. 13, pp. 2134–2140, 1974.
- [19] D. Crisp, S. Piazzolla, A. Biswas, "Mars Atmospheric Transmission Calculations", JPL R+TD FY07 Strategic Initiatives Mid-Year Review, April 06, 2007.

- [20] B. Moision, “The Capacity-Maximizing Field of View of an Optical Communications System”, IPN Progress Report 42-190, 2012.
- [21] D. Crisp, S. Piazzolla, A. Biswas, “Mars Upwelling Radiance Calculations”, JPL R+TD FY07 Strategic Initiatives Mid-Year Review, April 06, 2007.
- [22] E. Ku, A. Paletta, “Mission for an Impermanent Surface Stay to Investigate Our Neighbor, Mars”, AIAA ASCEND 2020-4086, 2020.
- [23] E. G. Lightsey, “Concept of operations for the visors mission: A two satellite cubesat formation flying telescope”, AAS Guidance, Navigation, and Control Conference 22-125, 2022.
- [24] P. Galchenko, “Attitude Determination and Control System Design for the GTOSat Mission”, AAS Guidance Navigation and Control Conference 23-031, 2023.
- [25] A. Paletta, “Development of an Autonomous Distributed Fault Management Architecture for the VISORS Mission”, Master’s Report, 2023.